

Dancing in the dark: galactic properties trace spin swings along the cosmic web

Y. Dubois^{1,2,3,4*}, C. Pichon^{1,2,4,5}, C. Welker^{1,2,3}, D. Le Borgne^{1,2}, J. Devriendt^{3,6}, C. Laigle^{1,2}, S. Codis^{1,2}, D. Pogosyan⁷, S. Arnouts⁸, K. Benabed^{1,2}, E. Bertin^{1,2}, J. Blaizot⁶, F. Bouchet^{1,2}, J.-F. Cardoso^{1,2}, S. Colombi^{1,2}, V. de Lapparent^{1,2}, V. Desjacques⁹, R. Gavazzi^{1,2}, S. Kassin¹⁰, T. Kimm¹¹, H. McCracken^{1,2}, B. Milliard⁸, S. Peirani^{1,2}, S. Prunet^{1,2,12}, S. Rouberol^{1,2}, J. Silk^{1,2,3,13}, A. Slyz³, T. Sousbie^{1,2}, R. Teyssier¹⁴, L. Tresse⁸, M. Treyer⁸, D. Vibert⁸ and M. Volonteri^{1,2,3,15}

(Affiliations can be found after the references)

Accepted 2014 June 19. Received 2014 June 19; in original form 2014 January 29

ABSTRACT

A large-scale hydrodynamical cosmological simulation, HORIZON-AGN, is used to investigate the alignment between the spin of galaxies and the cosmic filaments above redshift 1.2. The analysis of more than 150 000 galaxies per time step in the redshift range $1.2 < z < 1.8$ with morphological diversity shows that the spin of low-mass blue galaxies is preferentially aligned with their neighbouring filaments, while high-mass red galaxies tend to have a perpendicular spin. The reorientation of the spin of massive galaxies is provided by galaxy mergers, which are significant in their mass build-up. We find that the stellar mass transition from alignment to misalignment happens around $3 \times 10^{10} M_{\odot}$. Galaxies form in the vorticity-rich neighbourhood of filaments, and migrate towards the nodes of the cosmic web as they convert their orbital angular momentum into spin. The signature of this process can be traced to the properties of galaxies, as measured relative to the cosmic web. We argue that a strong source of feedback such as active galactic nuclei is mandatory to quench *in situ* star formation in massive galaxies and promote various morphologies. It allows mergers to play their key role by reducing post-merger gas inflows and, therefore, keeping spins misaligned with cosmic filaments.

Key words: methods: numerical — galaxies: evolution — galaxies: formation — galaxies: kinematics and dynamics — cosmology: theory — large-scale structure of Universe

1 INTRODUCTION

Theoretical models of structure formation by gravitational instability and numerical simulations have predicted that small fluctuations from the early Universe lead to the formation of a large-scale cosmic web made of clustered haloes, filaments, sheets and voids (e.g. Zeldovich et al. 1982; Klypin & Shandarin 1983; Blumenthal et al. 1984; Davis et al. 1985). The resulting properties of the Universe’s large-scale structure are the interplay of the planar local collapse, as emphasized in Zel’dovich (1970) (see also Shandarin & Zeldovich 1989) and the inherent struc-

ture of the Gaussian initial density and velocity shear fields, leading to the cosmic web picture of dense peaks connected by filaments, framing the honeycomb-like structure of walls (Bardeen et al. 1986; Bond et al. 1996).

The extension of the Center for Astrophysics redshift survey (Huchra et al. 1983) gave spectacular observational evidence (de Lapparent et al. 1986; Geller & Huchra 1989) for this picture, triggering a renewed interest for such large-scale galaxy surveys (Colless et al. 2001; Tegmark et al. 2004).

Modern simulations have established a tight connection between the geometry and dynamics of the large-scale structure of matter, on the one hand, and the evolution of the physical properties of forming galaxies, on the other. Obser-

* E-mail: dubois@iap.fr

vational information on the morphology of galaxies and its dependence on environment is routinely becoming available for galaxies up to redshift two and beyond (Abraham et al. 2007; Oesch et al. 2010; Lee et al. 2013). Matched samples at low and high redshifts allow for the study of the evolution of many physical properties of galaxies for most of the history of our Universe in unprecedented detail. A key question formulated decades ago is nevertheless not satisfactorily answered: what properties of galaxies are driven by the cosmic environment?

There is ample literature (e.g. Hoyle 1949; Peebles 1969; Doroshkevich 1970; White 1984; Schaefer 2009) on the tidal torque theory (TTT). It aims to explain the early acquisition of the spin¹ of haloes, in the regime where the dynamics is well described by the Zel'dovich approximation, and when it is legitimate to assume that the tidal and the inertia tensors are uncorrelated. Within this framework, TTT predicts that the spin of haloes should be perpendicular to the direction of filaments.

Using N -body simulations, which model only dark matter, Hahn et al. (2007) and Zhang et al. (2009) found halo spins preferentially oriented perpendicular to the filaments independent of halo mass. Hatton & Ninin (2001) claimed to detect an alignment between spin and filament, while Faltenbacher et al. (2002) measured a random orientation of the spins of haloes in the plane perpendicular to the filaments. More recently a consensus emerged when several works (Aubert et al. 2004; Bailin & Steinmetz 2005; Aragón-Calvo et al. 2007; Hahn et al. 2007; Paz et al. 2008; Sousbie et al. 2008; Libeskind et al. 2012; Trowland et al. 2013) reported that large-scale structures - filaments and sheets - influence the direction of the angular momentum of haloes in a way originally predicted by Sugerman et al. (2000) and Lee & Pen (2000). These studies pointed towards a mass-dependent orientation of the spin, arguing for the first time that the spin of high-mass haloes tends to lie perpendicular to their host filament, whereas low-mass haloes have a spin preferentially aligned with it. Nevertheless, the detected correlation remained weak and noisy until Codis et al. (2012) confirmed it. They quantified a redshift-dependent mass transition $M_{\text{tr,h}}$, separating aligned from perpendicular haloes, and interpreted the origin of the transition in terms of large-scale cosmic flows. Codis et al. (2012) found that high-mass haloes have their spins perpendicular to the filament because they are the results of mergers, a scenario suggested earlier by Aubert et al. (2004) (see also Bailin & Steinmetz 2005). Low-mass haloes are not the products of mergers and acquire their mass by gas accretion in the vorticity-rich neighbourhood of filaments, which explain why their spins are initially parallel to the filaments (Laigle et al. 2013; Libeskind et al. 2013).

Tempel et al. (2013) recently found tentative evidence of such alignments in the Sloan Digital Sky Survey (SDSS) with an orthogonality for elliptical galaxies and a weak alignment for spiral galaxies (see also Tempel & Libeskind 2013). Zhang et al. (2013) found that the major axis of red galaxies is parallel to their host filaments and is the same for blue galaxies albeit with a weaker signature. Similar mea-

surements have been done for galaxies and walls; there is evidence that the spin of galaxies also lies within the walls in which they are contained (Trujillo et al. 2006).

Besides those attempts to relate the spins of galaxies with the cosmic structure, much observational effort has been made to control the level of intrinsic alignments of galaxies as a potential source of systematic errors in weak gravitational lensing measurements (e.g. Croft & Metzler 2000; Heavens et al. 2000; Hirata & Seljak 2004). Such alignments are believed to be the major source of systematics of the future generation of lensing surveys like *Euclid* or Large Synoptic Survey Telescope (LSST). Direct measurements of the alignment of the projected light distribution of galaxies in wide-field imaging data seem to agree on a contamination at a level between a few per cent and ~ 10 per cent of the shear correlation functions, although the amplitude of the effect depends on the population of galaxies considered (e.g. Lee & Pen 2002; Joachimi et al. 2013). Given this dependence, it is difficult to use DM-only simulations as the sole resource to predict and control intrinsic alignments despite some success with the addition of a semi-analytical model prescription (e.g. Joachimi et al. 2013). The inherently anisotropic nature of the large-scale structure and its complex imprint on the shapes and spins of galaxies may prevent isotropic approaches from making accurate predictions.

Very few attempts have been made to probe the degree of correlation between *galaxy* spins and their embedding cosmic web using hydrodynamical cosmological simulations. Hahn et al. (2010) simulated the vicinity of a large-scale cosmic filament and found that – at odds with the results presented in our paper – the spin of galaxies within high-mass haloes is aligned with the filament while the spin of galaxies in low-mass haloes is perpendicular to the filament. Gay et al. (2010) focused on the colour gradients relative to the cosmic web using the HORIZON-MareNostrum simulation (Devriendt et al. 2010) which did not display much morphological diversity. They found evidence of metallicity gradients towards and along the filaments and nodes of the cosmic web. Danovich et al. (2012) also studied the feeding of massive galaxies at high redshift through cosmic streams using the HORIZON-MareNostrum simulation. They found that galaxies are fed by one dominant stream (with a tendency to be fed by three major streams), streams tend to be co-planar (in the stream plane), and that there is a weak correlation between spin of the galaxy and spin of the stream plane at the virial radius, which suggests an angular momentum exchange at the interface between streams and galaxies (see also Tillson et al. 2012).

In this paper, our focus is on the influence of the cosmic web as an anisotropic vector of the gas mass and angular momentum which ultimately shape galaxies. Our purpose is to determine if the mass-dependent halo spin-filament correlations of Codis et al. (2012) can be recovered via the morphology and physical properties of *simulated galaxies*. We aim to test these findings on a state-of-the-art hydrodynamical simulation, the so-called HORIZON-AGN simulation, which produced over 150 000 resolved galaxies displaying morphological diversity by redshift $z = 1.2$, in order to identify the effect of the environmentally driven spin acquisition on morphology and to probe the tendency of galaxies to

¹ Hereafter, the spin is the angular momentum unit vector for simplicity.

align or misalign with the cosmic filaments as a function of galactic properties.

The paper is organized as follows. Section 2 describes the numerical set-up of our simulation, the post-processing of galaxy properties and filament tracing. Section 3 presents the excess probability of alignment as a function of morphological tracers and investigates its redshift and spatial evolution. Section 4 discusses the origin of the observed (mis)alignment between galactic spins and filaments. We finally conclude in Section 5.

2 THE VIRTUAL DATA SET

In this section, we describe the HORIZON-AGN simulation (Section 2.1), how galaxies are identified in it, and how the virtual observables are derived (Section 2.2). We conclude this section with a description of the tools used to compare the spins of galaxies to the orientation of the cosmic web (Section 2.3).

2.1 The Horizon-AGN simulation

2.1.1 The code and initial conditions

We adopt a standard Λ cold dark matter cosmology with total matter density $\Omega_m = 0.272$, dark energy density $\Omega_\Lambda = 0.728$, amplitude of the matter power spectrum $\sigma_8 = 0.81$, baryon density $\Omega_b = 0.045$, Hubble constant $H_0 = 70.4 \text{ km s}^{-1} \text{ Mpc}^{-1}$, and $n_s = 0.967$ compatible with the Wilkinson Microwave Anisotropy Probe 7 cosmology (Komatsu et al. 2011). The values of this set of cosmological parameters are compatible with those of the recent *Planck* results within a 10 per cent relative variation (Planck Collaboration et al. 2013). The size of the box is $L_{\text{box}} = 100 h^{-1} \text{ Mpc}$ with 1024^3 DM particles, which results in a DM mass resolution of $M_{\text{DM, res}} = 8 \times 10^7 M_\odot$. The initial conditions have been produced with the MPGRAFIC software (Prunet et al. 2008). The simulation was run down to $z = 1.2$ and used 4 million CPU hours.

The HORIZON-AGN simulation is run with the adaptive mesh refinement code RAMSES (Teyssier 2002). The evolution of the gas is followed using a second-order unsplit Godunov scheme for the Euler equations. The HLLC Riemann solver (Toro et al. 1994) with MinMod total variation diminishing scheme is used to reconstruct the interpolated variables from their cell-centred values. Collisionless particles (DM and star particles) are evolved using a particle-mesh solver with a cloud-In-cell interpolation. The initial mesh is refined up to $\Delta x = 1 \text{ kpc}$ (seven levels of refinement). This is done according to a quasi-Lagrangian criterion: if the number of DM particles in a cell is more than 8, or if the total baryonic mass in a cell is eight times the initial DM mass resolution, a new refinement level is triggered. In order to keep the minimum cell size approximately constant in physical units, we allow a new maximum level of refinement every time the expansion scale factor doubles (i.e. at $a_{\text{exp}} = 0.1, 0.2, 0.4$ and 0.8).

2.1.2 Gas cooling and heating

Gas is allowed to cool by H and He cooling with a contribution from metals using a Sutherland & Dopita (1993) model down to 10^4 K . Heating from a uniform UV background takes place after redshift $z_{\text{reion}} = 10$ following Haardt & Madau (1996). Metallicity is modelled as a passive variable for the gas and its amount is modified by the injection of gas ejecta during supernova (SN) explosions and stellar winds. We also account for the release of various chemical elements synthesized in stars and released by stellar winds and SNe: O, Fe, C, N, Mg and Si. However, they do not contribute separately to the cooling curve (the ratio between each element is taken to be solar for simplicity) but can be used to probe the distribution of the various metal elements. The gas follows an equation of state for an ideal monoatomic gas with an adiabatic index of $\gamma = 5/3$.

2.1.3 Star formation and stellar feedback

The star formation process is modelled with a Schmidt law: $\dot{\rho}_* = \epsilon_* \rho / t_{\text{ff}}$, where $\dot{\rho}_*$ is the star formation rate (SFR) density, $\epsilon_* = 0.02$ (Kennicutt 1998; Krumholz & Tan 2007) the constant star formation efficiency and t_{ff} the local free-fall time of the gas. Star formation is allowed in regions which exceed a gas hydrogen number density threshold of $n_0 = 0.1 \text{ H cm}^{-3}$ following a Poissonian random process (Rasera & Teyssier 2006; Dubois & Teyssier 2008) with a stellar mass resolution of $M_* = \rho_0 \Delta x^3 \simeq 2 \times 10^6 M_\odot$. The gas pressure is artificially enhanced above $\rho > \rho_0$ assuming a polytropic equation of state $T = T_0 (\rho / \rho_0)^{\kappa-1}$ with polytropic index $\kappa = 4/3$ to avoid excessive gas fragmentation and mimic the effect of stellar heating on the mean temperature of the interstellar medium (Springel & Hernquist 2003). Feedback from stars is explicitly taken into account assuming a Salpeter (1955) initial mass function (IMF) with a low-mass (high-mass) cut-off of $0.1 M_\odot$ ($100 M_\odot$), as described in detail in Kimm et al. (in preparation). Specifically, the mechanical energy from Type II SNe and stellar winds is taken from STARBURST99 (Leitherer et al. 1999, 2010), and the frequency of Type Ia SN explosions is computed following Greggio & Renzini (1983).

2.1.4 Feedback from black holes

The same ‘canonical’ active galactic nuclei (AGN) feedback modelling employed in Dubois et al. (2012) is used here. Black holes (BHs) are created where the gas mass density is larger than $\rho > \rho_0$ with an initial seed mass of $10^5 M_\odot$. In order to avoid the formation of multiple BHs in the same galaxy, BHs are not allowed to form at distances less than 50 kpc from each other. The accretion rate on to BHs follows the Bondi–Hoyle–Lyttleton rate $\dot{M}_{\text{BH}} = 4\pi\alpha G^2 M_{\text{BH}}^2 \bar{\rho} / (\bar{c}_s^2 + \bar{u}^2)^{3/2}$, where M_{BH} is the BH mass, $\bar{\rho}$ is the average gas density, \bar{c}_s is the average sound speed, \bar{u} is the average gas velocity relative to the BH velocity, and α is a dimensionless boost factor with $\alpha = (\rho / \rho_0)^2$ when $\rho > \rho_0$ and $\alpha = 1$ otherwise (Booth & Schaye 2009) in order to account for our inability to capture the colder and higher density regions of the interstellar medium. The effective accretion rate on to BHs is capped at the Eddington accretion rate: $\dot{M}_{\text{Edd}} = 4\pi G M_{\text{BH}} m_p / (\epsilon_* \sigma_T c)$, where σ_T

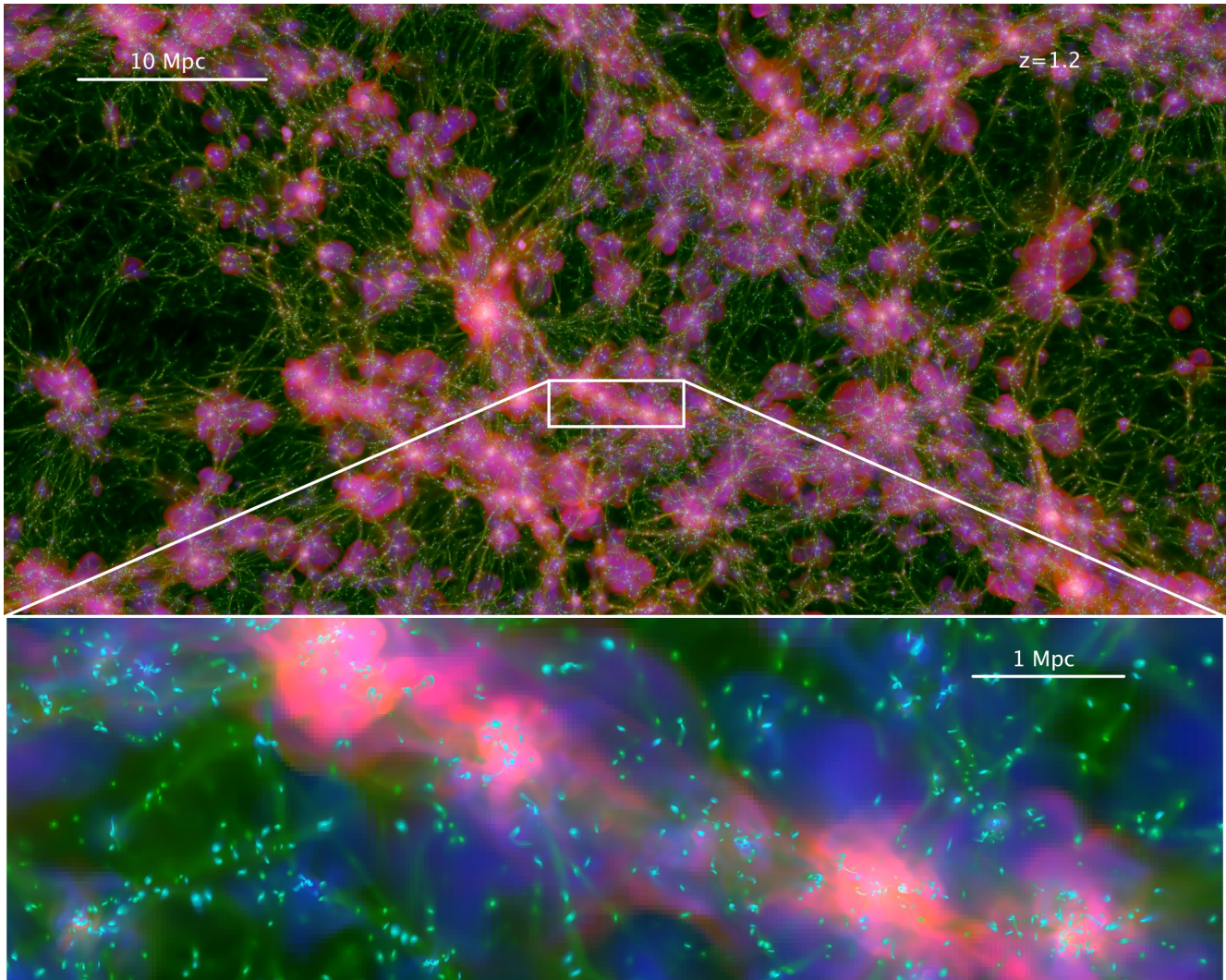


Figure 1. Projected maps of the HORIZON-AGN simulation at $z = 1.2$ are shown. Gas density (green), gas temperature (red) and gas metallicity (blue) are depicted. The top image is $100 h^{-1}$ Mpc across in comoving distance and covers the whole horizontal extent of the simulation and $25 h^{-1}$ Mpc comoving in depth. The bottom image is a sub-region where we see thin cosmic filaments as well as thicker filaments several Mpc long bridging shock-heated massive haloes and surrounded by a metal-enriched intergalactic medium. Physical scales are indicated on the figures in proper units.

is the Thompson cross-section, c is the speed of light, m_p is the proton mass and ϵ_r is the radiative efficiency, assumed to be equal to $\epsilon_r = 0.1$ for the Shakura & Sunyaev (1973) accretion on to a Schwarzschild BH.

The AGN feedback is a combination of two different modes, the so-called *radio* mode operating when $\chi = \dot{M}_{\text{BH}}/\dot{M}_{\text{Edd}} < 0.01$ and the *quasar* mode active otherwise. The quasar mode consists of an isotropic injection of thermal energy into the gas within a sphere of radius Δx , and at an energy deposition rate: $\dot{E}_{\text{AGN}} = \epsilon_f \epsilon_r \dot{M}_{\text{BH}} c^2$. In this equation, $\epsilon_f = 0.15$ is a free parameter chosen to reproduce the scaling relations between BH mass and galaxy properties (mass, velocity dispersion) and BH density in our local Universe (see Dubois et al. 2012). At low accretion rates, the radio mode deposits AGN feedback energy into a bipolar outflow with a jet velocity of 10^4 km s^{-1} . The outflow is modelled as a cylinder with a cross-sectional radius Δx and height $2 \Delta x$ following Omma et al. (2004) (more details

are given in Dubois et al. 2010). The efficiency of the radio mode is larger than the quasar mode with $\epsilon_f = 1$.

A projected map of half the simulation volume and a smaller subregion is shown in Fig. 1. Gas density, gas temperature and gas metallicity are depicted. One can discern the large-scale pattern of the cosmic web, with filaments and walls surrounding voids and connecting haloes. Massive haloes are filled with hot gas, and feedback from SNe and AGN pours warm and metal-rich gas in the diffuse intergalactic medium. As demonstrated in Dubois et al. (2013), the modelling of AGN feedback is critical to create early-type galaxies and provide the sought morphological diversity (see Fig. 2 for a snippet of the galaxy sample of the simulation) in hydrodynamical cosmological simulations (see e.g. Croton et al. 2006, for semi-analytical models).

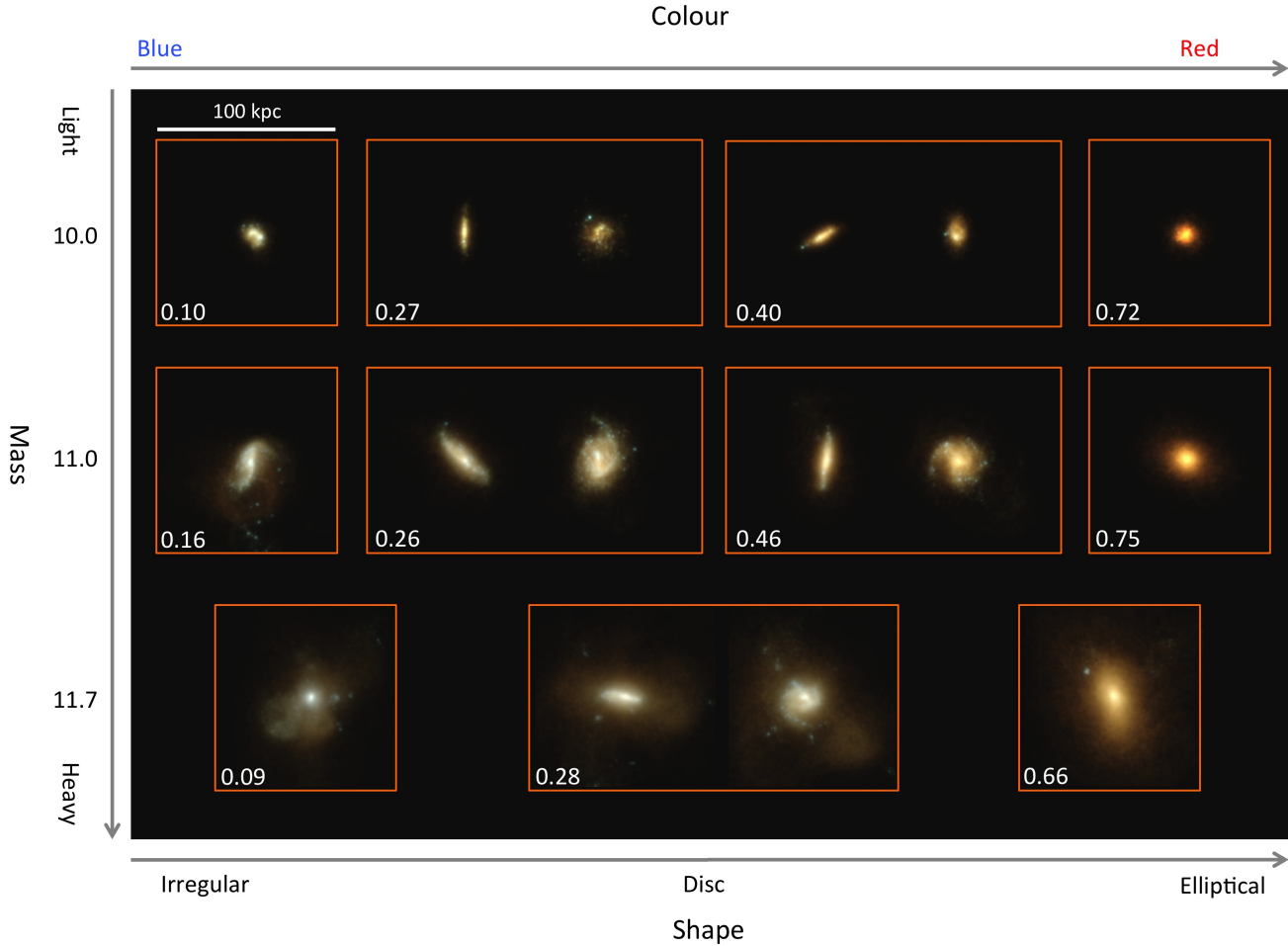


Figure 2. Stellar emission of a sample of galaxies in the HORIZON-AGN simulation at $z = 1.3$ observed through rest-frame u , g and i filters. Extinction by dust is not taken into account. Each vignette size is 100 kpc vertically. The numbers on the left of the figure indicate the galaxy stellar mass in log solar mass units. The number in the bottom left of each vignette is the $g - r$ rest-frame colour, not corrected for dust extinction. Disc galaxies (galaxies in the centre of the figure) are shown edge-on and face-on.

2.2 Mock observations of galaxies

We describe how we produce various observables that can be compared qualitatively with data from modern observational surveys. In this paper we focus on observables which are known to correlate with the Hubble type of galaxies, namely mass, V/σ , colour, morphological parameters like Gini and M_{20} , and age.

2.2.1 Identifying and segmenting galaxies

Galaxies are identified with the AdaptaHOP finder (Aubert et al. 2004, updated to its recent version by Tweed et al. 2009 for building merger trees) which directly operates on the distribution of star particles. A total of 20 neighbours are used to compute the local density of each particle, a local threshold of $\rho_t = 178$ times the average total matter density is applied to select relevant densities, and the force softening (minimum size below which substructures are considered irrelevant) is ~ 2 kpc. Only galactic structures identified with more than 50 particles are considered. It allows for a clear separation

of galaxies (defined as sets of star particles segmented by AdaptaHOP), including those in the process of merging. Catalogues of around $\sim 150\,000$ galaxies are produced for each redshift analysed in this paper from $z = 3$ to 1.2.

2.2.2 Synthetic colours

We compute the absolute AB magnitudes and rest-frame colours of galaxies using single stellar population models from Bruzual & Charlot (2003) assuming a Salpeter IMF. Each star particle contributes to a flux per frequency that depends on its mass, age, and metallicity. The sum of the contribution from all stars is passed through the u , g , r and i filters from the SDSS. Fluxes are expressed as rest-frame quantities (i.e. that do not take into account the red-shifting of spectra). We also neglect the contribution to the reddening of spectra from internal (interstellar medium) or external (intergalactic medium) dust extinction. Once the flux in each waveband is obtained for a star particle, we build two-dimensional projected maps from single galaxies (satellites are excised with the galaxy finder), and we can sum up the

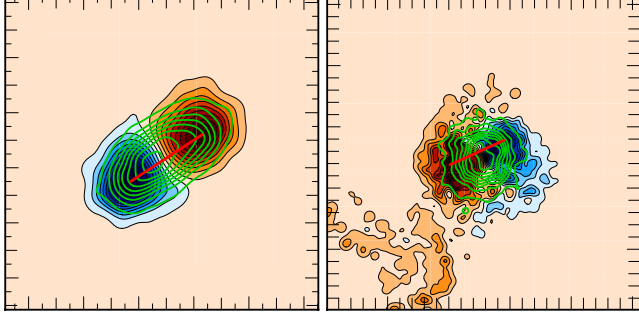


Figure 3. Example of integral field spectroscopy for the velocity of a fast rotator $V/\sigma > 1$ (left-hand panel) and a slow rotator $V/\sigma < 1$ (right-hand panel). The thick red line corresponds to the position of the slit, which is placed along the kinetic major axis. The green iso-contours correspond to the velocity dispersion map. The size of the images is 50 kpc and the mean velocity (respectively dispersion) amplitude is 150 (respectively 75) km s^{-1} (left-hand panel) and 50 (respectively 100) km s^{-1} (right-hand panel).

total contribution of their stars to the total luminosity. A small sample of galaxies representative of the morphological variety in the simulation is shown in Fig. 2.

2.2.3 Projected stellar kinematics

For each galaxy, we build a field of view centred on the galaxy, which is made of 256×256 pixels over 100 kpc size (corresponding to a pixel size of 0.4 kpc or 0.05 arcsec at $z = 1.83$). We compute the luminosity-weighted velocity along the line of sight (arbitrary defined as the x -axis of the simulation):

$$\bar{v}_{\text{pixel}} = \frac{\sum_i v_{\text{los},i} I_{i,\text{filter}}}{\sum_i I_{i,\text{filter}}}, \quad (1)$$

where $v_{\text{los},i}$ is the velocity along the line of sight of the i -th star in the pixel considered and $I_{i,\text{filter}}$ is the intensity in the corresponding filter bandwidth (u, g, r, i) of the i -th star in the pixel considered. Then, the velocity dispersion along the line of sight is:

$$\bar{\sigma}_{\text{pixel}}^2 = \frac{\sum_i v_{\text{los},i}^2 I_{i,\text{filter}}}{\sum_i I_{i,\text{filter}}} - \bar{v}_{\text{pixel}}^2. \quad (2)$$

The velocity maps are then smoothed with a Gaussian kernel of 15 pixels. The position of the fastest (respectively slowest) pixel, which defines V for that galaxy, is then identified automatically and a 0.75 arcsec “slit” is put across so as to interpolate through the kinematic major axis of the galaxy. The smoothed velocity dispersion map is also interpolated along the same axis and the maximum of that curve defines σ (see Fig. 3 for example of a slow and a fast rotator). V/σ is then straightforwardly the corresponding ratio.

2.2.4 Specific star formation rate

The calculation of the SFR is done on stars as identified by the galaxy finder that belong to a given galaxy. To compute the SFR, we compute the amount of stars formed over the last 100 Myr. The choice of 100 Myr corresponds to a minimum measurable SFR of $M_*/100 \text{ Myr} = 0.02 M_\odot \text{ yr}^{-1}$.

The specific star formation rate (sSFR) is then calculated by dividing the SFR by the galaxy stellar mass, M_* .

2.2.5 Gini and M_{20}

The morphology of each galaxy is often measured by two non-parametric parameters: the Gini (G , Abraham et al. 2003) and M_{20} (Lotz et al. 2004). The Gini parameter is a non-parametric measure of the inequality of fluxes in pixels, ranging from zero (for a perfectly uniform image) to unity (for an image with all the flux in one pixel, for instance). M_{20} is the second order momentum of light of the 20 per cent brightest pixels of a galaxy. It traces the spatial distribution of any bright nuclei, bars, spiral arms, and off-centre star clusters. As shown in Lotz et al. (2004), galaxies with $M_{20} > -1.1$ mainly are extended objects with double or multiple nuclei, whereas low values of M_{20} (< -1.6) are relatively smooth with a bright nucleus. Both parameters are known to correlate well with the concentration parameter (Abraham et al. 1994) for regular shapes, but they are better suited for disturbed morphologies because of their non-parametric nature. These two parameters have been used to characterize observations in the local universe and at high redshift (e.g. Lotz et al. 2004; Abraham et al. 2007; Wang et al. 2012; Lee et al. 2013) and they are well suited to analyse large samples of galaxies of mixed morphologies. In the local universe, galaxies with a high Gini value and a low M_{20} value are mainly ellipticals, whereas late-type galaxies and irregular have lower G and larger M_{20} values. Mergers tend to have large G and large M_{20} values.

Images in the i band are obtained from a segmentation of 3D objects with the galaxy finder. The images are rebinned to 64×64 pixels for a 100 kpc size image in order to avoid star particles appearing as individual pixels. Then, as in Lee et al. (2013), we measure the Petrosian radius with an elliptical aperture which is obtained as in SEXTRACTOR (Bertin & Arnouts 1996) from the second-order moment of light. The Petrosian semi-major axis a_p is such that the ratio of the surface brightness at a_p over the mean surface brightness within a_p is decreasing at a_p and becomes smaller than 0.2. In practice, we fit a spline to the surface brightness ratio profile and find the zero of the function $\mu(a_p)/\mu(< a_p) - 0.2$. Galaxies with a_p smaller than 2 pixels are filtered out: they are almost always associated with low-mass galaxies ($M_* < 10^{9.2} M_\odot$) with few star particles, and the G and M_{20} parameters are very uncertain for these objects. We also filter out galaxies less massive than $M_* < 10^{9.5} M_\odot$ for which we suffer the most from resolution effects. A description of the bivariate distributions of G , M_{20} and stellar mass is given in Appendix A.

2.2.6 Ages

The mean ages of galaxies are obtained through the summation of the mass-weighted age of star particles belonging to the galaxy.

2.2.7 Spin of galaxies

To compute the spin of galaxies, we compute the total angular momentum of their stars with respect to the particle of

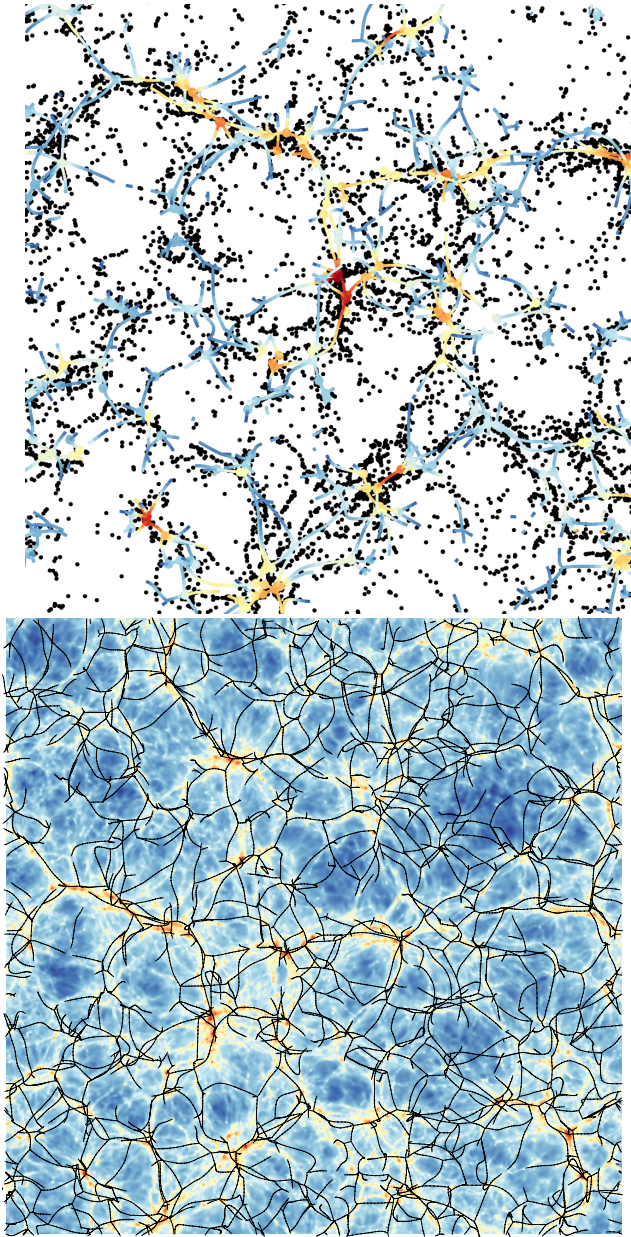


Figure 4. Top: projection along the z -axis of the HORIZON-AGN gas skeleton (colour coded by logarithmic density as red–yellow–blue–white from high density to low density) at redshift $z = 1.83$ of a slice of $25 h^{-1}$ Mpc on the side and $10 h^{-1}$ Mpc thickness. Galaxies are superimposed as black dots. The clustering of the galaxies follows the skeleton quite closely. Bottom: larger view of the skeleton on top of the projected gas density. This paper quantifies orientation of the galaxies relative to the local anisotropy set by the skeleton.

maximum density (centre of the galaxy) from the smoothed stellar density constructed with the AdaptaHOP algorithm.

We have also tested the effect of grid-locking on the Cartesian axes of the box (a common issue of Cartesian-based Poisson solvers for which a numerical anisotropy in the force calculation arises; see e.g. Hockney & Eastwood 1981) in Appendix B for galaxies and filaments.

2.3 Tracing large-scale structures via the skeleton

In order to quantify the orientation of galaxies relative to the cosmic web, we use a geometric three-dimensional ridge extractor well suited to identify filaments, called the ‘skeleton’. A gas density cube of 512^3 pixels is drawn from the simulation and Gaussian-smoothed with a length of $3 h^{-1}$ Mpc comoving chosen so as to trace large-scale filamentary features. Two implementations of the skeleton, based on ‘watershed’ (Sousbie et al. 2009) and ‘persistence’ (Sousbie et al. 2011), were implemented, without significant difference for the purpose of this investigation. The first method identifies ridges as the boundaries of walls which are themselves the boundaries of voids. The second one identifies ridges as the ‘special’ lines connecting topologically robust (filament-like) saddle points to peaks.

Fig. 4 shows a slice of $25 h^{-1}$ Mpc of the skeleton colour coded by logarithmic density, along with galaxies contained within that slice. The clustering of the galaxies follows quite closely the skeleton of the gas, i.e. the cosmic filaments. Note that, on large scales, the skeleton built from the gas is equivalent to that built from the DM as the gas and DM trace each other closely. The rest of the paper is devoted to studying the orientation of the spin of these galaxies relative to the direction of the nearest skeleton segment. In practice, an octree is built from the position of the mid-segment of the skeleton to speed up the association of the galaxy position to its nearest skeleton segment. It was checked that our results were not sensitive to how many such segments were considered to define the local direction of the skeleton. The orientation of the segment of the skeleton is used to define the relative angle between the filament and the spin of the galaxy. The segments are also tagged with their curvilinear distance to the closest node (where different filaments merge), which allows us to study the evolution of this (mis)alignment *along* the cosmic web. Appendix B investigates the effect of grid-locking of the skeleton’s segments in the HORIZON-AGN simulation. Large-scale filaments, defined from the skeleton, do not show any alignment with the grid.

3 SPIN SWING EVOLUTION

This paper focuses on the orientation of the spin of galaxies relative to the filaments in which they are embedded and the cosmic evolution. Specifically, we aim to see if its evolution can be traced via physical and morphological tracers. We investigate in Section 3.1 how this orientation varies with different tracers of the Hubble type of galaxies, namely stellar mass, V/σ , sSFR, colour, metallicity, age, M_{20} and Gini on our sample of 150 000 galaxies. Afterwards, in Section 3.2, we quantify how this alignment varies as a function of distance to the filaments and along the filaments to the nodes of the cosmic web. We study the cosmic evolution of the alignment of the spin of galaxies and filaments in Section 3.3.

3.1 Alignment of galaxies and filaments

We measure the statistical signature of the (mis)alignment of galaxies with their closest filament segment. The alignment is defined as the angle θ between the spin of the stellar

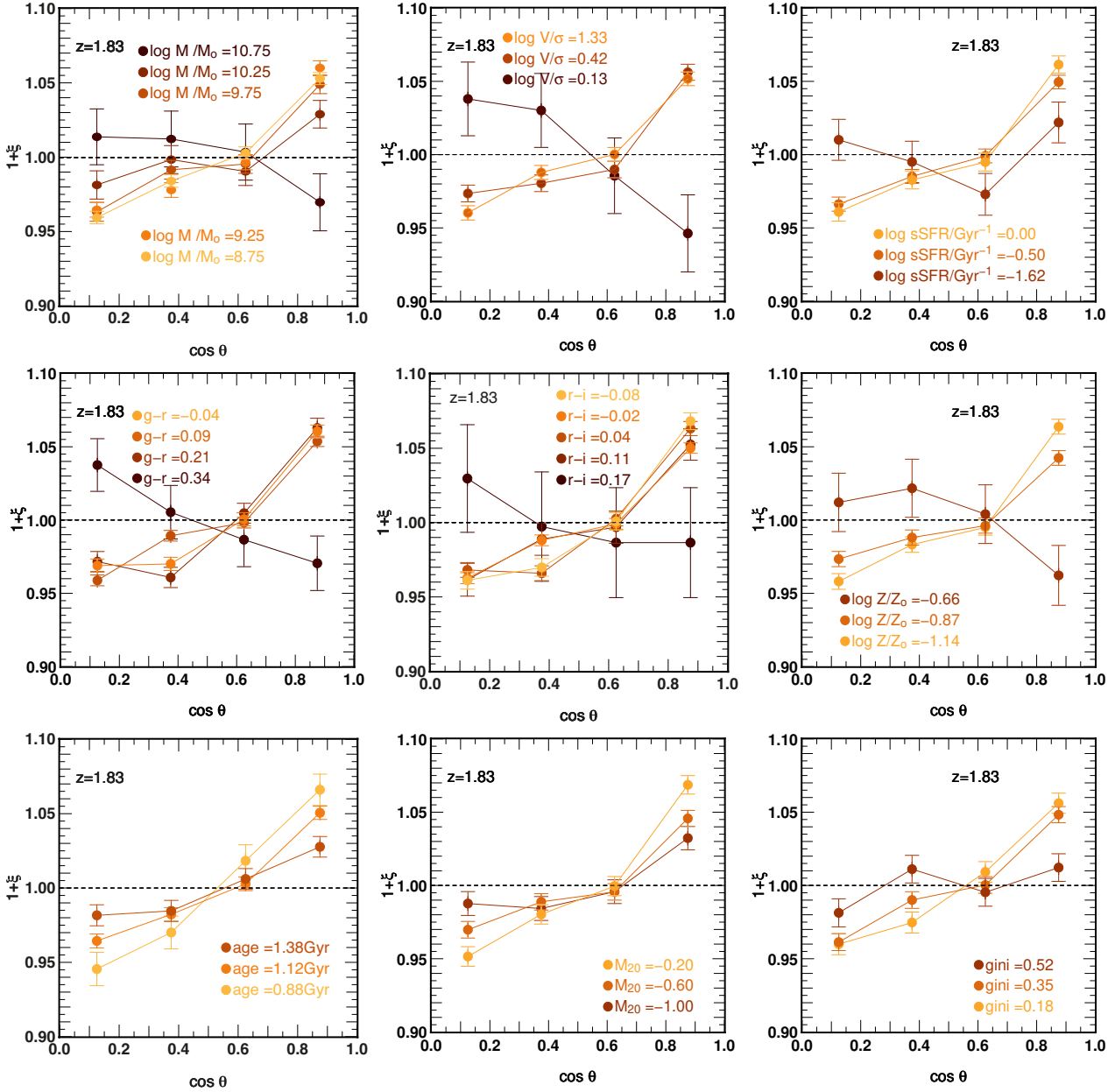


Figure 5. Excess probability, ξ , of the alignment between the spin of galaxies and their closest filament is shown as a function of galaxy properties at $z = 1.83$: M_s (top row, left column), V/σ (top row, middle column), sSFR (top row, right column), $g - r$ (middle row, left column), $r - i$ (middle row, middle column), metallicity Z (middle row, right column), age (bottom row, left column), M_{20} (bottom row, middle column) and Gini (bottom row, right column). Half-sigma error bars are shown for readability. Dashed line is uniform PDF (excess probability $\xi = 0$). Massive, dispersion-dominated, passive, red, smooth and old galaxies tend to have a spin perpendicular or randomly oriented with the direction of their filament. Low-mass, centrifugally supported, star-forming, blue, irregular and young galaxies tend to align with the direction of their closest filament.

component and the direction of the filamentary segment. Recall that the spin of the galaxy is obtained by removing merging substructures using the galaxy finder, and computing the net angular momentum of its stars with respect to its centre (defined as the point of highest stellar density). Note that the filament segments are assumed to have no polarity. Hence we impose the angle θ has a $\pi/2$ symmetry, and is expressed in terms of $\cos \theta = [0, 1]$.

Fig. 5 shows the resulting probability density function (PDF), $1 + \xi$, at $z = 1.83$, where ξ is the excess probability of

$\cos \theta$ in bins of various quantities: mass, kinematics, sSFR, colour, metallicity, age, M_{20} and Gini. A uniform PDF (i.e. random orientations of galaxies relative to their filament) is represented as a dashed line for comparison. Galaxies with mass below $M_s < 10^9 M_\odot$ are removed from the calculation, except for investigation of alignment as a function of mass.

More massive galaxies tend to have their spin preferentially perpendicular to their filament, while less massive ones have their spin preferentially parallel. A transition occurs around a stellar mass of $M_{\text{tr},s} = 3 \times 10^{10} M_\odot$. This value is

fully consistent with earlier findings of a mass transition for the orientation of the spin of haloes of $M_{\text{tr,h}} = 5 \times 10^{11} M_{\odot}$ at that redshift (Codis et al. 2012) and suggested by the galaxy–halo mass relation determined by abundance matching techniques (Moster et al. 2013). Using the full redshift sample, Fig. 6 shows that the mass transition appears to be reasonably bracketed at $M_{\text{tr,s}} \simeq 10^{10.5 \pm 0.25} M_{\odot}$. The mean values of the PDF $1 + \xi$ at $\cos \theta = 0.9$ are, respectively, 0.98 and 1.02 for $M_s = 10^{10.75} M_{\odot}$ and $10^{10.25} M_{\odot}$.

The definition of Hubble type relies on different tracers. Hence, it is of interest to quantify the alignment or misalignment of galaxies classified according to these tracers. One should keep in mind that these tracers are not independent from one another (as illustrated in Appendix A). Top row, middle column of Fig. 5 shows the excess probability of alignment for V/σ . Dispersion-dominated galaxies with small V/σ ratios (i.e. elliptical galaxies) have their spin perpendicular to filaments, while centrifugally supported galaxies with large V/σ (i.e. disc galaxies) have their spins parallel to filaments. The transition between parallel and perpendicular alignment occurs at $V/\sigma = 0.6$. A similar signal, not represented here, is found for intrinsic (three-dimensional) kinematics. The top-right panel of Fig. 5 shows ξ as a function of the sSFR of galaxies. Intense star-forming galaxies that rejuvenate their stellar mass content in less than $1/\text{sSFR} = 1/10^{-0.5} \simeq 3 \text{ Gyr}$ tend to align with filaments. Conversely, galaxies that are passive ($\text{sSFR} \simeq 0.1 \text{ Gyr}^{-1}$) show a random orientation of their spin relative to the filaments. The left and central panels of the middle row of Fig. 5 shows ξ as a function of the $g-r$ and the $r-i$ colours of galaxies, respectively. Redder galaxies ($g-r > 0.25$ or $r-i > 0.13$) have their spin perpendicular to their filaments, while bluer galaxies ($g-r \leq 0.25$ or $r-i \leq 0.13$) have their spin parallel to them. The right-hand panel of the middle row of Fig. 5 shows ξ as a function of the stellar metallicity Z . Metal-poor galaxies are more aligned with filaments than metal-rich galaxies which tend to be misaligned. The bottom-left panel of Fig. 5 shows ξ as a function of the galaxy age. Older galaxies have their spin more randomly oriented with that of the filaments, and young galaxies with age below $\simeq 1.2 \text{ Gyr}$ exhibit a stronger alignment. Finally, the bottom-middle and bottom-right panels of Fig. 5 show ξ as a function of the M_{20} and Gini quantitative morphological indices. Galaxies with high M_{20} are more aligned with filaments than galaxies with low M_{20} . Galaxies with low Gini are more aligned with filaments than galaxies with high Gini. Galaxies with low M_{20} and high Gini tend to trace elliptical galaxies (Lotz et al. 2008). Note that for age, M_{20} and Gini, galaxies in the HORIZON-AGN simulation do not seem to present enough leverage to identify a complete misalignment (in contrast to the other tracers).

To summarize, massive, dispersion-dominated, passive, red, smooth, metal-rich and old galaxies tend to have a spin perpendicular or randomly oriented to filaments. In contrast, low-mass, centrifugally supported, star-forming, blue, irregular, metal-poor and young galaxies tend to align with filaments.

The transitions presented here are more indicative of a trend than a definite proof that each tracer yields a precise morphological transition. Amongst the various tracers, V/σ and $g-r$ are those for which the transition from alignment to perpendicular misalignment is the most significant. Yet

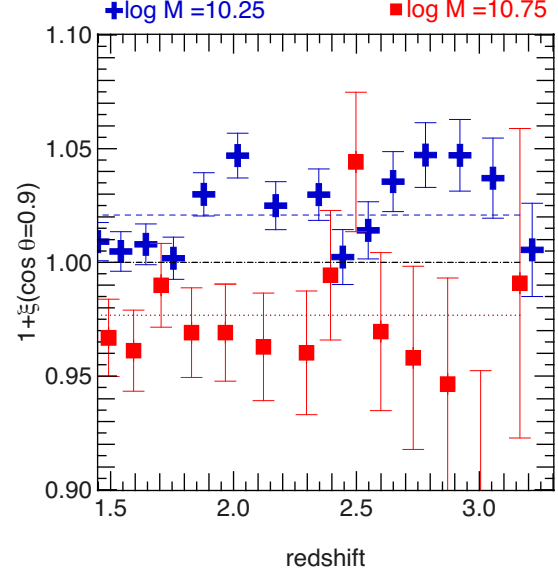


Figure 6. Average values of $1 + \xi(\cos \theta = 0.9)$ as a function of redshift for two different bins of stellar mass $M_s = 10^{10.25}$ (pluses) and $M_s = 10^{10.75}$ (squares). Errors bars correspond to half-sigma error. The dotted (respectively dashed) lines correspond to the mean of the lower (respectively higher) bin mass. The mean values of $1 + \xi(\cos \theta = 0.9)$ are 0.975 for stellar mass $M_s = 10^{10.75}$ and 1.023 for $M_s = 10^{10.25}$, respectively. The transition mass seems reasonably bracketed at $M_{\text{tr,s}} = 10^{10.5 \pm 0.25} M_{\odot}$.

the ensemble allows us to have confidence in the underlying physical picture as they are all consistent with the expected variations. The above mentioned consistent analysis of its redshift evolution (Fig. 6) brings further confidence in our results. It should also be noted that each estimator is derived from a fairly crude automated analysis.

3.2 Spin orientation along the cosmic web

We now investigate the orientation of the alignment as a function of the distance to filaments and nodes. The upper panel of Fig. 7 shows the evolution of alignment of the spin of galaxies as a function of distance to the closest filament for a low-mass subsample. We apply this measurement to low-mass galaxies because they lie in filaments, sheets and voids, while the most massive galaxies are usually located at the intersection of the most massive filaments in the most massive haloes, therefore, with a minimum scatter in distance to filaments. Galaxies closer to filaments have their spin more parallel. The lower panel of Fig. 7 shows the evolution of alignment of the spin of galaxies as a function of distance to nodes (i.e. where filaments intersect) along the filaments. Galaxies further away from nodes have their spin more parallel than galaxies closer to nodes. This is consistent with the idea that galaxies merge while drifting along filaments (which destroys alignment), and with the strong colour (curvilinear) gradients found by Gay et al. (2010).

3.3 Redshift evolution

We now investigate the redshift evolution of the excess probability of alignment. We post-process the HORIZON-AGN in

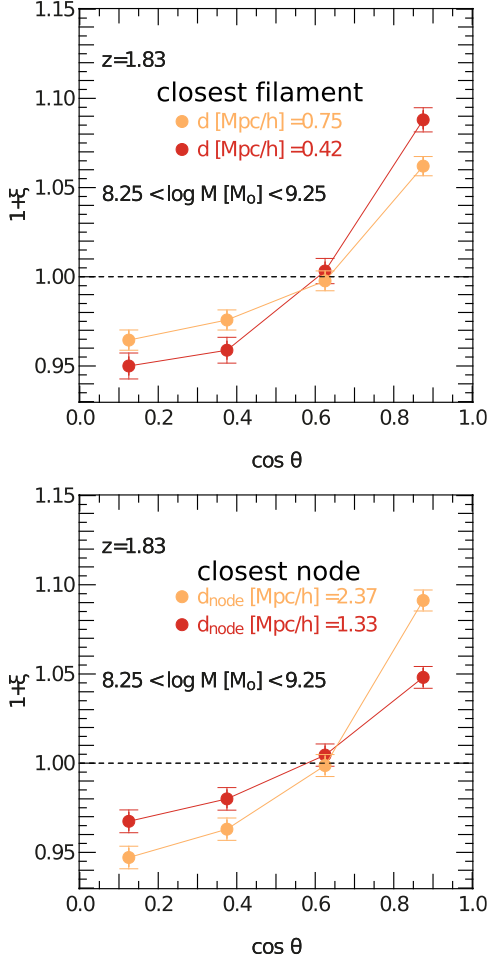


Figure 7. Excess probability ξ of the alignment between the spin of galaxies and their closest filament as a function of their distance to the closest filament (top panel) or node (bottom panel) is shown at $z = 1.83$. Galaxies closer to filaments have their spin more parallel, while galaxies closer to nodes are more randomly oriented. Dashed line is the zero excess probability $\xi = 0$.

the following redshift range: $z = 3.01 - 1.23$. Fig. 8 shows the amplitude of the alignment of the spin of all galaxies as a function of redshift. The PDF shows that, on average, galaxies are aligned with their neighbouring filament, because low-mass galaxies dominate in number over massive galaxies (because the mass function of galaxies is strongly decreasing with mass). The amplitude of the alignment decreases with cosmic time (decreasing redshift) which is a result of more galaxies evolving passively (i.e. for a given mass, the SFR decreases with time). The lower the redshift, the stronger the amount of shell crossing and cumulative contribution from mergers along the filaments which tend to destroy the existing alignment and convert orbital momentum into spin to orient it perpendicular to that of the host filament.

4 DISCUSSION: AGN FEEDBACK PROMOTES SPIN SWINGS?

The above analysis suggests that the most massive galaxies, which are also the reddest, the oldest, the most metal-rich

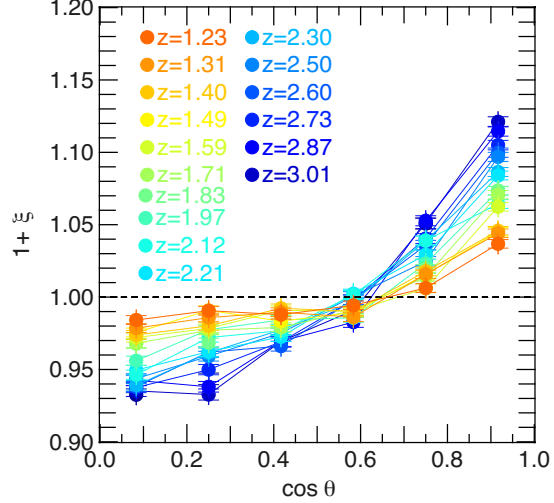


Figure 8. Excess probability ξ of the alignment between the spin of galaxies (with mass above $10^8 M_\odot$) and their closest filament as a function of redshift is shown. Dashed line is the zero excess probability $\xi = 0$. The amplitude of the correlation shows an alignment which increases with redshift (i.e. decreases with cosmic time).

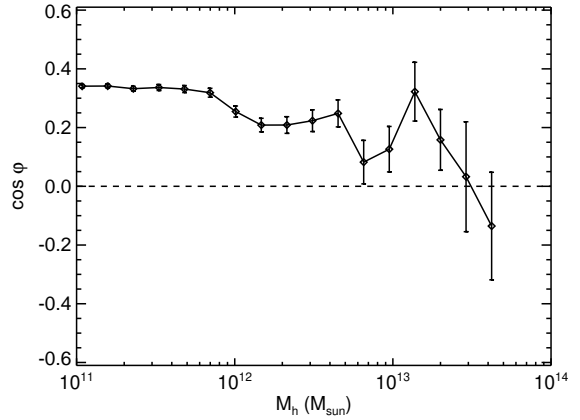


Figure 9. Average cosine of the angle $\cos \psi$ between the galaxy angular momentum and that of its host halo as a function of the halo mass at $z = 1.3$ (solid line). Error bars are the standard errors of the mean. Note that the random distribution (dashed line) is for $\cos \psi = 0$ because vectors can be pointing towards different directions and, therefore, galaxy spin and halo spin can be aligned or anti-aligned.

and the most pressure-supported, tend to have their spin perpendicular to the axis of filaments. Galaxies on average also show less alignment with time (i.e. with decreasing redshift). We argue that the origin of the misalignment is the sudden reorientation of galactic angular momentum during mergers. This was shown in Codis et al. (2012) to be the case for the origin of the DM halo–filament misalignment for massive haloes. Misalignment occurs because orbital momentum is converted into spin, as DM haloes catch up each other *along* the filaments. We also argue that indirect merger rate indicators, such as those presented in Section 2.2 (galaxy properties), can only be modelled once an efficient feedback

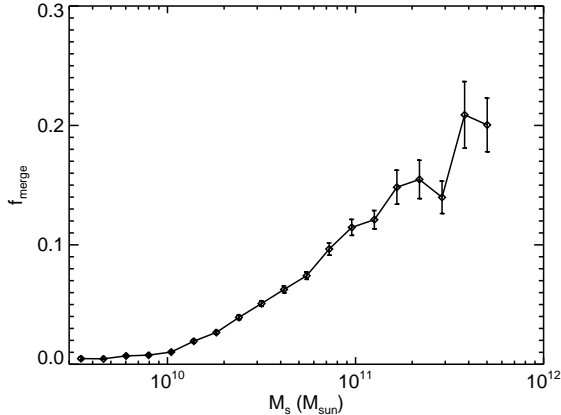


Figure 10. Average fraction of stellar mass gained through mergers as a function of the galaxy stellar mass at $z = 1.83$. The error bars are the standard errors on the mean. More massive galaxies have a larger fraction of galaxy mergers contributing to their stellar mass. Lower mass galaxies build up their stellar mass through *in situ* star formation only.

mechanism is implemented to produce morphological and physical diversity.

4.1 The contribution of cosmic dynamics

Massive galaxies undergo mergers (minor and major) that contribute to misalignment of their spin with respect to the direction of the filament. Given the level of significance for this range of galaxy mass (compatible with a uniform PDF at less than $1\text{-}\sigma$ for $M_s \simeq 10^{10.75} M_{\odot}$, see the top-left panel of Fig. 5), it is still unclear whether massive galaxies have as strong a preference for a spin orientation perpendicular to the axis of their neighbouring filament as do their halo counterparts, or if they tend to be randomly oriented.

First, note that, globally, the excess probability of alignment is always at values $\xi \lesssim 0.1$ (Figs 5, 7 and 8), therefore, the signal is weak (not all galaxies align or misalign) but statistically significant. For instance, the (mis)alignment signal between haloes and filaments (Codis et al. 2012) or that between the large-scale vorticity and filaments (Laigle et al. 2013) are respectively of somewhat (~ 15 per cent) and significantly (~ 100 per cent) larger amplitudes. One could expect that small scales (i.e. galaxies) decouple more strongly from the large-scale filaments than the intermediate scales (i.e. haloes), which are the first virialized structures. In particular, there could be a significant amount of redistribution of angular momentum within the inner regions of haloes (Kimm et al. 2011; Dubois et al. 2012; Danovich et al. 2012; Kassin et al. 2012; Kassin et al. 2012; Tillson et al. 2012), and as a consequence, galaxies misalign with the spin of their host halo (see Fig. 9 for the average cosine of the angle ψ between the angular momentum of the galaxy and that of the host halo), while they keep a strong alignment with the spin of the dark halo’s central region (Hahn et al. 2010). On the other hand, low-mass central galaxies are fed angular momentum directly by cold flows (Pichon et al. 2011; Tillson et al. 2012), which connects them more tightly to their cosmic environment than one would naively expect.

The orientation and amplitude of the stellar component itself reflect the corresponding cumulative advection of cold gas directly on to the circumgalactic medium. In contrast, the orientation of the spin of haloes is more sensitive to the latest stochastic accretion events at the virial radius. The net outcome of both competing processes, as traced by the physical properties of galaxies, is summarized in Figs 5 and 6.

Fig. 9 shows that, because of the above-mentioned redistribution of angular momentum within the inner region of the halo, the galactic spin is weakly correlated to that of the whole halo, and the effect is more pronounced for more massive haloes which merge more frequently. Satellites end up reaching the central galaxy with less correlated orbital angular momentum even though they globally originate from a preferred direction, as set by the cosmic web. In order to test this hypothesis, we build merger trees from the catalogue of galactic structures detected by our galaxy finder. For each galaxy, we measure the stellar mass acquired through the different branches of the tree (satellites) that we quote as a merger, the main progenitor being excluded from the calculation. Fig. 10 shows that massive galaxies acquire a non-negligible fraction of their mass by mergers (at least 1000 particles of star particles, up to 20 per cent at $z = 1.83$), while low-mass galaxies grow their stellar mass content almost exclusively by *in situ* star formation (e.g. De Lucia & Blaizot 2007; Oser et al. 2010). Fig. 11 shows examples of the evolution of the spin orientation for six massive galaxies, $4 \times 10^{10} \lesssim M_s \lesssim 2 \times 10^{11} M_{\odot}$. They have a significant contribution from mergers to their stellar mass, which play a significant role in shaping their spin orientations (Bett & Frenk 2012). In Fig. 11, the fraction of mass gained by mergers $\delta M_{\text{merge}}/M_s$ between two time steps is indicated by dashed blue lines. When no mergers happen, galaxies keep a steady spin direction. It is only when a companion galaxy is captured ($\delta M_{\text{merge}}/M_s \neq 0$) do we see a sudden reorientation of the spin. An investigation of the relative role of minor, major, dry and wet mergers is postponed to a companion paper (Welker et al. 2014) which shows unambiguously that major mergers are indeed responsible for important spin swings.

In contrast to high-mass galaxies, low-mass galaxies have their spins preferentially aligned with that of their closest filaments. Gas embedded within large-scale walls streams into the filaments which bound them, winding up to form the first generation of galaxies which have spins parallel to these filaments (Pichon et al. 2011). Since these galaxies build up their stellar mass *in situ* without significant external perturbations, the stars retain the angular momentum of the cold gas obtained directly from the cosmic web. Fig. 12 shows the excess probability of the cosine of the angle μ between the vorticity of the gas (as estimated on scales of $200 h^{-1} \text{ kpc}$) at the galaxy’s position and the direction of the spin of galaxies (dominated by the low-mass population). As was found in Laigle et al. (2013) for the spin of DM haloes (see also Libeskind et al. 2013), the galactic spin is also strongly correlated with the vorticity of the surrounding gas. This correlation has polarity: there are fewer galaxies with their spin anti-aligned with the local vorticity. This dynamical and stellar evidence therefore allows us to apply to baryons the scenario presented in Laigle et al. (2013)

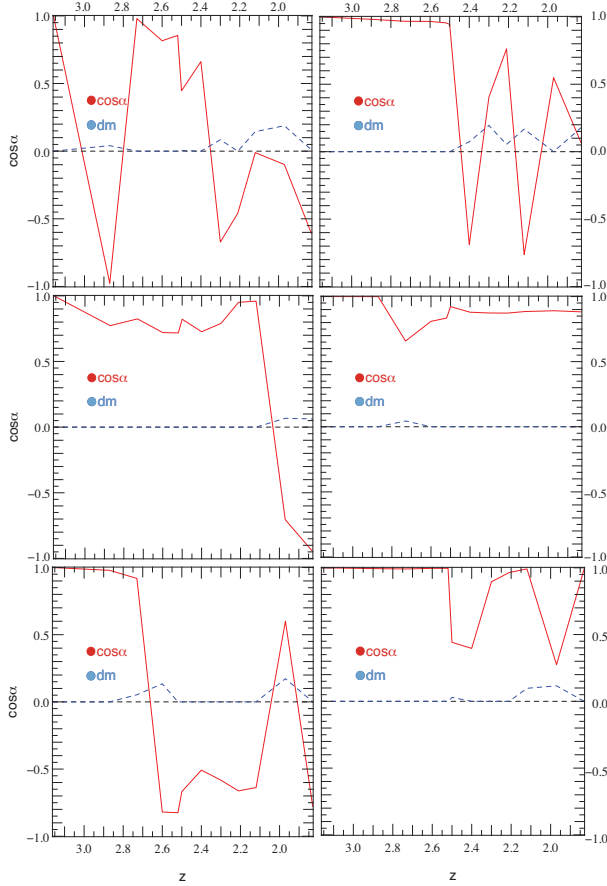


Figure 11. Examples of galaxies changing their spin direction during mergers with stellar mass $1.7 \times 10^{11} M_\odot$ (top left), $7.3 \times 10^{10} M_\odot$ (top right), $3.8 \times 10^{10} M_\odot$ (middle left), $4.8 \times 10^{10} M_\odot$ (middle right), $1.2 \times 10^{11} M_\odot$ (bottom left) and $6.0 \times 10^{10} M_\odot$ (bottom right) at $z = 1.83$. $\cos \alpha$ (red curve) is the cosine of the angle between the spin of the galaxy at the current redshift and the initial spin measured at $z = 3.15$. The differential fraction of mass between two time steps coming from mergers $dm = \delta M_{\text{merge}}/M_s$ (in blue) is overplotted. Non-zero values correspond to rapid changes in spin direction. In the absence of mergers, the galaxy spin has a steady direction.

on the vorticity-driven origin of the galactic spin–filament alignment.

4.2 The contribution of AGN feedback

Fig. 13 shows the stellar halo mass relation at $z = 1.3$ for the HORIZON-AGN simulation. It appears that above $M_h \gtrsim 10^{12} M_\odot$ the relation is in good agreement with abundance-matching results from Moster et al. (2013). Note that the stellar masses from Moster et al. (2013) are rescaled by +0.19 dex to account for a change from Kroupa to Salpeter IMF. The presence of the feedback from AGN reduces the amount of stars formed in these massive galaxies, allowing them to agree with observations by reducing the stellar mass up to one order of magnitude (Dubois et al. 2013; Puchwein & Springel 2013; Martizzi et al. 2014). Note also that the transition mass from alignment to misalignment is close to the mass ($\simeq 10^{11} M_\odot$) where passive galaxies become more abundant than star-forming galax-

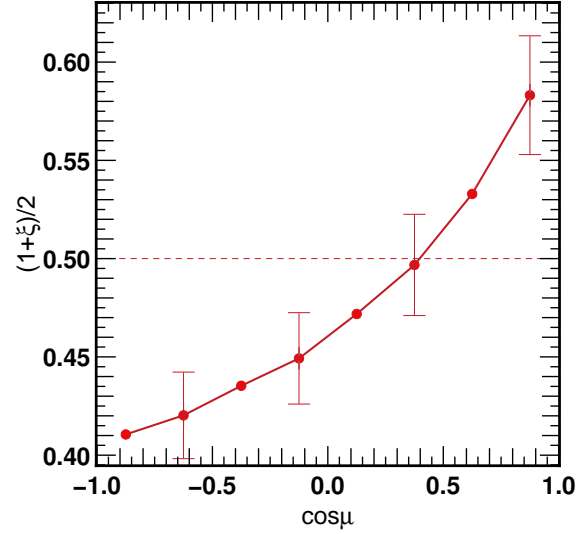


Figure 12. Excess probability ξ of the cosine of the angle μ between the vorticity of the gas and the direction of the spin of the galaxies at $z = 1.83$. The dashed line indicates no correlation. Vorticity is computed as the curl of the velocity field, after a Gaussian smoothing of the velocity field with a kernel length of $780 h^{-1} \text{kpc}$. Note that fewer galaxies are anti-aligned. Error bars are the standard errors of the mean.

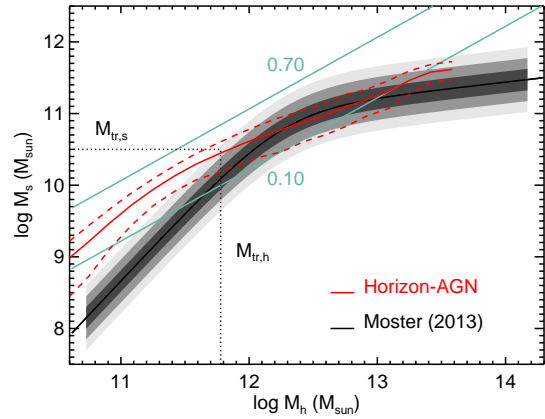


Figure 13. Average stellar mass of the central galaxy as a function of the host halo mass in the simulation at $z = 1.3$ (red curve) with the 1σ dispersion together with the abundance matching result from Moster et al. (2013) at the same redshift assuming a Salpeter IMF (+0.19 dex in stellar mass from Kroupa to Salpeter IMF) with the 1σ , 2σ and 3σ error bars represented by the shaded areas. The cyan lines indicate constant stellar efficiencies defined as $f_{\text{eff}} = M_s/(\Omega_b/\Omega_m M_h)$. The transition mass between alignment and misalignment of the galaxy ($M_{\text{tr},s}$), respectively, halo ($M_{\text{tr},h}$), spin and the filament are represented as dotted lines.

ies in observations (Drory et al. 2009; Davidzon et al. 2013; Ilbert et al. 2013). For massive galaxies, mergers are key in both swinging the spin *and* changing the morphology. The sSFR decreases significantly with galaxy stellar mass (see Fig. 14) because of the quenching of their gas accretion rate – in the shock-heated mode of accretion for massive haloes (e.g. Birnboim & Dekel 2003; Ocvirk et al. 2008;

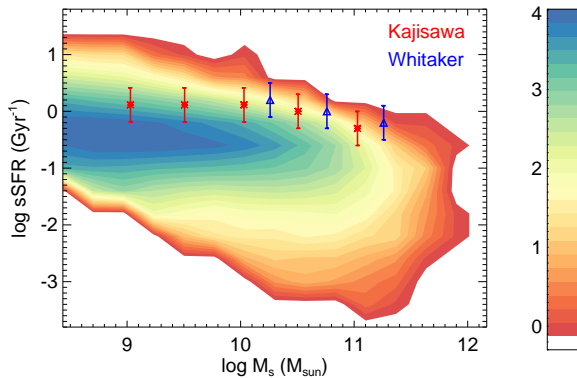


Figure 14. Diagram of the distribution of galaxies as a function of their sSFR and stellar mass M_s at $z = 1.3$. The contours are the number of galaxies in log units. Red and blue points with error bars are the observations at $z = 1.25$ extracted from Behroozi et al. (2013) and originally from Kajisawa et al. (2010) and Whitaker et al. (2012) and rescaled for a Salpeter IMF (+0.26 dex in stellar mass from Chabrier to Salpeter IMF). The sSFR decreases with galaxy stellar mass.

Dekel et al. 2009) – and because of the strong suppression of cold gas within galaxies via AGN feedback. Observational data from Behroozi et al. (2013) at $z = 1.3$ (originally from Kajisawa et al. 2010 and Whitaker et al. 2012) are represented on top of the distribution of our simulations points. Stellar masses from Behroozi et al. (2013) are rescaled by +0.26 dex to account for a change from Chabrier to Salpeter IMF. The quenching of the SFR in massive galaxies through AGN feedback leads to an enhanced fraction of stars gained through mergers (Dubois et al. 2013). For lower mass galaxies, the agreement of the stellar halo mass relation with observational data is less favourable because feedback from SNe is not strong enough to suppress the star formation in dwarfs. Some missing physical processes, such as radiation from young stars, are probably necessary to further suppress the star formation in low-mass galaxies (e.g. Hopkins et al. 2011; Murray et al. 2011; Hopkins et al. 2013). Vogelsberger et al. (2013) manage to reproduce the low-mass tail of the stellar-to-halo mass relation by decoupling hydrodynamically the launched wind gas from the dense star-forming gas (as introduced by Springel & Hernquist 2003). This decoupling of gas is known to generate a more efficient transfer of energy from SNe to large-scale galactic winds, compared to local prescriptions as we have adopted here (as shown by Dalla Vecchia & Schaye 2008), but it lacks physical motivation. Note that the choice of the Salpeter IMF instead of a Chabrier IMF decreases the total energy released by a stellar particle by a factor of 3 (assuming a minimum and maximum mass of $0.1 M_\odot$ and $100 M_\odot$). However, we are still confident that stronger feedback in low-mass galaxies should not drastically change their orientation, since mergers for that class of haloes are rare enough (Fakhouri et al. 2010; Genel et al. 2010). This is in particular true for the major mergers that are required to significantly reorient the spins of galaxies (Welker et al. 2014).

The significant contribution from AGN feedback at re-

ducing the stellar activity in massive galaxies is mandatory to obtain a diversity in the physical properties of galaxies (colours, V/σ , sSFR, etc.) across the whole mass range (see Appendix A). The effect of AGN feedback is to also reduce the mass of stars formed *in situ*, i.e. to prevent the formation of a rotation-supported component in massive galaxies and to turn massive galaxies into pressure-supported ellipticals (Dubois et al. 2013). In the absence of a central supermassive BH, the magnitude of the angular momentum of the stellar component of massive galaxies will therefore be larger, as a larger fraction of their (larger) stellar mass will be distributed in a rotationally supported disc. Thus, a merging satellite the angular momentum of which is misaligned with that of the central galaxy produces a variation in the angle between the pre-merger and the post-merger spin of the galaxy that is smaller for the disc case (no AGN case) than for the elliptical case (AGN case). Moreover, for massive galaxies, the feedback from the central AGN switches off later accretion of circumgalactic gas (Dubois et al. 2010). Consequently, the possible realignment of the galactic spin with the filament that could operate after a merger due the accretion of fresh gas is reduced by the presence of the AGN feedback from the galaxy remnant. AGN feedback thereby acts as a catalyst of spin swings.

5 CONCLUSIONS

Our analysis of the HORIZON-AGN flagship simulation, which models AGN as well as stellar feedback so as to produce morphological diversity, shows that the orientation of the spin of galaxies depends on various galaxy properties such as stellar mass, V/σ , sSFR, M_{20} , metallicity, colour and age. The spins of galaxies tend to be preferentially parallel to their neighbouring filaments, for low-mass, young, centrifugally supported, metal-poor, bluer galaxies, and perpendicular for higher mass, higher velocity dispersion, red, metal-rich old galaxies. The alignment is the strongest, the closer to the filaments and further from the nodes of the cosmic web the galaxies are. This is in agreement with the predictions of Codis et al. (2012) for DM haloes. We find a transition mass, $M_{\text{tr},s} \simeq 3 \times 10^{10} M_\odot$ which is also consistent with these authors' predictions for the corresponding halo transition mass. Due to the weak galaxy–halo alignment, the amplitude of the correlation with cosmic filaments is somewhat weaker for galaxies than for haloes. It also decreases with cosmic time due to mergers and quenching of cold flows and star formation. Hence, our results suggest that galaxy properties can be used to trace the spin swings along the cosmic web.

The transition from the aligned to the misaligned case is dynamically triggered by mergers (the frequency of which increases with galaxy mass) that swing the spin of galaxies. AGN feedback has a key role at preventing further gas inflow and quenching the *in situ* star formation after such an event, in order to preserve the misalignment operated by the merger.

Though it is expected that galaxy modelling will improve over the next decade – in particular the way feedback is taken into account in large-scale cosmological simulations – we do not anticipate that the particular results found in this paper should change qualitatively. The finding that the

morphological diversity of galaxies traces populations with different spin–filament alignments, which in turn is in part inherited from the anisotropy of the embedding cosmic web, is both robust predictions of the current gravitational clustering scenario and of our understanding of the dynamics of elliptical and spiral galaxies.

In a forthcoming paper, we will analyse more realistic mock catalogues from the HORIZON-AGN light-cone down to a lower redshift to investigate the amount of modification of the signal induced by dust extinction, projection effects, limited resolution and finite signal-to-noise ratio. More efficient and robust estimators for morphology, either intrinsic using the full data set of the simulation or projected using virtual degraded observables, will be built and compared. Quantitative comparisons to observations are postponed to this paper.

ACKNOWLEDGEMENTS

We thank the anonymous referee for suggestions, which improved the clarity of the paper. This work has made use of the HPC resources of CINES (Jade supercomputer) under the allocation 2013047012 made by GENCI. The post-processing made use of the *horizon* and *Dirac* clusters. This work is partially supported by the Spin(e) grants ANR-13-BS05-0002 of the French *Agence Nationale de la Recherche* and by the National Science Foundation under Grant No. NSF PHY11-25915. This research is part of the Horizon-UK project. YD and CP thank the KITP for hospitality when this project was initiated. CP also thanks the institute of Astronomy for a Sacker visiting fellowship and the PEPS ‘Physique théorique et ses interfaces’ for funding. The research of YD and JS has been supported at IAP by ERC project 267117 (DARK) hosted by Université Pierre et Marie Curie - Paris 6. YD is grateful to the Beecroft Institute for Particle Astrophysics and Cosmology for hospitality and to the Balzan Foundation for support, at Oxford University where some of this work was carried out. The research of JS has also been supported at the Johns Hopkins University by National Science Foundation grant OIA-1124403. The research of AS and JD at Oxford is supported by the Oxford Martin School and Adrian Beecroft. This work was also supported by the ILP LABEX (under reference ANR-10-LABX-63) was supported by French state funds managed by the ANR within the Investissements d’Avenir programme under reference ANR-11-IDEX-0004-02. We thank D. Munro for freely distributing his YORICK programming language and opengl interface (available at <http://yorick.sourceforge.net/>).

References

Abraham R. G., Nair P., McCarthy P. J., Glazebrook K., et al. 2007, *ApJ*, 669, 184
 Abraham R. G., Valdes F., Yee H. K. C., van den Bergh S., 1994, *ApJ*, 432, 75
 Abraham R. G., van den Bergh S., Nair P., 2003, *ApJ*, 588, 218
 Aragón-Calvo M. A., van de Weygaert R., Jones B. J. T., van der Hulst J. M., 2007, *ApJ Let.*, 655, L5

Aubert D., Pichon C., Colombi S., 2004, *MNRAS*, 352, 376
 Bailin J., Steinmetz M., 2005, *ApJ*, 627
 Bardeen J. M., Bond J. R., Kaiser N., Szalay A. S., 1986, *ApJ*, 304, 15
 Behroozi P. S., Wechsler R. H., Conroy C., 2013, *ApJ*, 770, 57
 Bertin E., Arnouts S., 1996, *Astronomy and Astrophysics Supplement Series*, 117, 393
 Bett P. E., Frenk C. S., 2012, *MNRAS*, 420, 3324
 Birnboim Y., Dekel A., 2003, *MNRAS*, 345, 349
 Blumenthal G. R., Faber S. M., Primack J. R., Rees M. J., 1984, *Nature*, 311, 517
 Bond J. R., Kofman L., Pogosyan D., 1996, *Nature*, 380, 603
 Booth C. M., Schaye J., 2009, *MNRAS*, 398, 53
 Bruzual G., Charlot S., 2003, *MNRAS*, 344, 1000
 Codis S., Pichon C., Devriendt J., Slyz A., Pogosyan D., Dubois Y., Sousbie T., 2012, *MNRAS*, 427, 3320
 Colless M., Dalton G., Maddox S., et al. 2001, *MNRAS*, 328, 1039
 Croft R. A. C., Metzler C. A., 2000, *ApJ*, 545, 561
 Croton D. J., Springel V., White S. D. M., De Lucia G., Frenk C. S., Gao L., Jenkins A., Kauffmann G., Navarro J. F., Yoshida N., 2006, *MNRAS*, 365, 11
 Dalla Vecchia C., Schaye J., 2008, *MNRAS*, 387, 1431
 Danovich M., Dekel A., Hahn O., Teyssier R., 2012, *MNRAS*, 422, 1732
 Davidzon I., Bolzonella M., Coupon J., Ilbert O., Arnouts S., et al. 2013, *A&A*, 558, A23
 Davis M., Efstathiou G., Frenk C. S., White S. D. M., 1985, *ApJ*, 292, 371
 de Lapparent V., Geller M. J., Huchra J. P., 1986, *ApJ Let.*, 302, L1
 De Lucia G., Blaizot J., 2007, *MNRAS*, 375, 2
 Dekel A., Birnboim Y., Engel G., et al. 2009, *Nature*, 457, 451
 Devriendt J., Rimes C., Pichon C., et al. 2010, *MNRAS*, 403, L84
 Doroshkevich A. G., 1970, *Astrophysics*, 6, 320
 Drory N., Bundy K., Leauthaud A., et al. 2009, *ApJ*, 707, 1595
 Dubois Y., Devriendt J., Slyz A., Teyssier R., 2010, *MNRAS*, 409, 985
 Dubois Y., Devriendt J., Slyz A., Teyssier R., 2012, *MNRAS*, 420, 2662
 Dubois Y., Gavazzi R., Peirani S., Silk J., 2013, *MNRAS*, 433, 3297
 Dubois Y., Pichon C., Haehnelt M., Kimm T., Slyz A., Devriendt J., Pogosyan D., 2012, *MNRAS*, 423, 3616
 Dubois Y., Teyssier R., 2008, *A&A*, 477, 79
 Fakhouri O., Ma C.-P., Boylan-Kolchin M., 2010, *MNRAS*, 406, 2267
 Faltenbacher A., Gottlöber S., Kerscher M., Müller V., 2002, *A&A*, 395, 1
 Gay C., Pichon C., Le Borgne D., Teyssier R., Sousbie T., Devriendt J., 2010, *MNRAS*, 404, 1801
 Geller M. J., Huchra J. P., 1989, *Science*, 246, 897
 Genel S., Bouché N., Naab T., Sternberg A., Genzel R., 2010, *ApJ*, 719, 229
 Greggio L., Renzini A., 1983, *A&A*, 118, 217
 Haardt F., Madau P., 1996, *ApJ*, 461, 20
 Hahn O., Carollo C. M., Porciani C., Dekel A., 2007, *MNRAS*, 375, 1000

- RAS*, 381, 41
- Hahn O., Porciani C., Carollo C. M., Dekel A., 2007, *MNRAS*, 375, 489
- Hahn O., Teyssier R., Carollo C. M., 2010, *MNRAS*, 405, 274
- Hatton S., Ninin S., 2001, *MNRAS*, 322, 576
- Heavens A., Refregier A., Heymans C., 2000, *MNRAS*, 319, 649
- Hirata C. M., Seljak U., 2004, *Phys. Rev. D*, 70, 063526
- Hockney R. W., Eastwood J. W., 1981, *Computer Simulation Using Particles*
- Hopkins P. F., Keres D., Onorbe J., Faucher-Giguere C.-A., Quataert E., Murray N., Bullock J. S., 2013, ArXiv e-prints
- Hopkins P. F., Quataert E., Murray N., 2011, *MNRAS*, 417, 950
- Hoyle F., 1949, *Problems of Cosmical Aerodynamics*, Central Air Documents, Office, Dayton, OH. Central Air Documents Office, Dayton, OH
- Huchra J., Davis M., Latham D., Tonry J., 1983, *ApJ Sup.*, 52, 89
- Ilbert O., McCracken H. J., Le Fevre O., Capak P., Dunlop J., et al. 2013, *A&A*, 556, A55
- Joachimi B., Semboloni E., Bett P. E., Hartlap J., Hilbert S., Hoekstra H., Schneider P., Schrabback T., 2013, *MNRAS*, 431, 477
- Kajisawa M., Ichikawa T., Yamada T., Uchimoto Y. K., Yoshikawa T., Akiyama M., Onodera M., 2010, *ApJ*, 723, 129
- Kassin S. A., Devriendt J., Fall S. M., de Jong R. S., Allgood B., Primack J. R., 2012, *MNRAS*, 424, 502
- Kassin S. A., Weiner B. J., Faber S. M., Gardner J. P., et al. 2012, *ApJ*, 758, 106
- Kennicutt Jr. R. C., 1998, *ApJ*, 498, 541
- Kimm T., Devriendt J., Slyz A., Pichon C., Kassin S. A., Dubois Y., 2011, ArXiv e-prints
- Klypin A. A., Shandarin S. F., 1983, *MNRAS*, 204, 891
- Komatsu E., Smith K. M., Dunkley J., et al. 2011, *ApJ Sup.*, 192, 18
- Krumholz M. R., Tan J. C., 2007, *ApJ*, 654, 304
- Laigle C., Pichon C., Codis S., Dubois Y., et al. 2013, ArXiv e-prints
- Lee B., Giavalisco M., Williams C. C., Guo Y., et al. 2013, *ApJ*, 774, 47
- Lee J., Pen U., 2000, *ApJ*, 532, L5
- Lee J., Pen U.-L., 2002, *ApJ Let.*, 567, L111
- Leitherer C., Ortiz Otálvaro P. A., Bresolin F., Kudritzki R.-P., Lo Faro B., Pauldrach A. W. A., Pettini M., Rix S. A., 2010, *ApJ Sup.*, 189, 309
- Leitherer C., Schaerer D., Goldader J. D., et al. 1999, *ApJ Sup.*, 123, 3
- Libeskind N. I., Hoffman Y., Forero-Romero J., Gottlöber S., Knebe A., Steinmetz M., Klypin A., 2013, *MNRAS*, 428, 2489
- Libeskind N. I., Hoffman Y., Knebe A., Steinmetz M., Gottlöber S., Metuki O., Yepes G., 2012, *MNRAS*, 421, L137
- Libeskind N. I., Hoffman Y., Steinmetz M., Gottlöber S., Knebe A., Hess S., 2013, *ApJ Let.*, 766, L15
- Lotz J. M., Davis M., Faber S. M., et al. 2008, *ApJ*, 672, 177
- Lotz J. M., Primack J., Madau P., 2004, *AJ*, 128, 163
- Martizzi D., Mohammed I., Teyssier R., Moore B., 2014, *MNRAS*, 440, 2290
- Moster B. P., Naab T., White S. D. M., 2013, *MNRAS*, 428, 3121
- Murray N., Ménard B., Thompson T. A., 2011, *ApJ*, 735, 66
- Ocvirk P., Pichon C., Teyssier R., 2008, *MNRAS*, 390, 1326
- Oesch P. A., Carollo C. M., Feldmann R., et al. 2010, *ApJ*, 714, L47
- Omma H., Binney J., Bryan G., Slyz A., 2004, *MNRAS*, 348, 1105
- Oser L., Ostriker J. P., Naab T., Johansson P. H., Burkert A., 2010, *ApJ*, 725, 2312
- Paz D. J., Stasyszyn F., Padilla N. D., 2008, *MNRAS*, 389, 1127P
- Peebles P. J. E., 1969, *ApJ*, 155, 393
- Pichon C., Pogosyan D., Kimm T., Slyz A., Devriendt J., Dubois Y., 2011, *MNRAS*, pp 1739+
- Planck Collaboration Ade P. A. R., Aghanim N., Armitage-Caplan C., Arnaud M., Ashdown M., Atrio-Barandela F., Aumont J., Baccigalupi C., Banday A. J., et al. 2013, ArXiv e-prints
- Prunet S., Pichon C., Aubert D., Pogosyan D., Teyssier R., Gottloeber S., 2008, *ApJ Sup.*, 178, 179
- Puchwein E., Springel V., 2013, *MNRAS*, 428, 2966
- Rasera Y., Teyssier R., 2006, *A&A*, 445, 1
- Salpeter E. E., 1955, *ApJ*, 121, 161
- Schaefer B. M., 2009, *International Journal of Modern Physics D*, 18, 173
- Shakura N. I., Sunyaev R. A., 1973, *A&A*, 24, 337
- Shandarin S. F., Zeldovich Y. B., 1989, *Reviews of Modern Physics*, 61, 185
- Sousbie T., Colombi S., Pichon C., 2009, *MNRAS*, 393, 457
- Sousbie T., Pichon C., Colombi S., Pogosyan D., 2008, *MNRAS*, 383, 1655
- Sousbie T., Pichon C., Kawahara H., 2011, *MNRAS*, 414, 384
- Springel V., Hernquist L., 2003, *MNRAS*, 339, 289
- Sugerman B., Summers F. J., Kamionkowski M., 2000, *MNRAS*, 311, 762
- Sutherland R. S., Dopita M. A., 1993, *ApJ Sup.*, 88, 253
- Tegmark M., Blanton M. R., Strauss M. A., et al. 2004, *ApJ*, 606, 702
- Tempel E., Libeskind N. I., 2013, *ApJ Let.*, 775, L42
- Tempel E., Stoica R. S., Saar E., 2013, *MNRAS*, 428, 1827
- Teyssier R., 2002, *A&A*, 385, 337
- Tillson H., Devriendt J., Slyz A., Miller L., Pichon C., 2012, ArXiv e-prints
- Toro E. F., Spruce M., Speares W., 1994, *Shock Waves*, 4, 25
- Trowland H. E., Lewis G. F., Bland-Hawthorn J., 2013, *ApJ*, 762, 72
- Trujillo I., Carretero C., Patiri S. G., 2006, *ApJ Let.*, 640, L111
- Tweed D., Devriendt J., Blaizot J., Colombi S., Slyz A., 2009, *A&A*, 506, 647
- Vogelsberger M., Genel S., Sijacki D., Torrey P., Springel V., Hernquist L., 2013, *MNRAS*, 436, 3031
- Wang T., Huang J.-S., Faber S. M., Fang G., et al. 2012, *ApJ*, 752, 134
- Welker C., Devriendt J., Dubois Y., Pichon C., Peirani S., 2014, ArXiv e-prints

- Whitaker K. E., van Dokkum P. G., Brammer G., Franx M., 2012, *ApJ Let.*, 754, L29
 White S. D. M., 1984, *ApJ*, 286, 38
 Zeldovich I. B., Einasto J., Shandarin S. F., 1982, *Nature*, 300, 407
 Zel'dovich Y. B., 1970, *A&A*, 5, 84
 Zhang Y., Yang X., Faltenbacher A., Springel V., Lin W., Wang H., 2009, *ApJ*, 706, 747
 Zhang Y., Yang X., Wang H., Wang L., Mo H. J., van den Bosch F. C., 2013, *ApJ*, 779, 160

- ¹ Sorbonne Universités, UPMC Univ Paris 06, UMR 7095, Institut d'Astrophysique de Paris, F-75005 Paris, France
² CNRS, UMR 7095, Institut d'Astrophysique de Paris, 98 bis Boulevard Arago, F-75014 Paris, France
³ Sub-department of Astrophysics, University of Oxford, Keble Road, Oxford OX1 3RH, UK
⁴ KITP Kohn Hall, 4030 University of California Santa Barbara, CA 93106-4030, USA
⁵ Institute of Astronomy and Kavli Institute for Cosmology, Madingley Road, Cambridge CB3 0HA, UK
⁶ Observatoire de Lyon, UMR 5574, 9 avenue Charles André, F-69561 Saint Genis Laval, France
⁷ Department of Physics, University of Alberta, 11322-89 Avenue, Edmonton, Alberta T6G 2G7, Canada
⁸ Aix Marseille Université, CNRS, Laboratoire d'Astrophysique de Marseille, UMR 7326, 38 rue F. Joliot-Curie, 13388 Marseille, France
⁹ Département de Physique Théorique, Université de Genève 24 quai Ernest Ansermet, CH-1211 Genève, Switzerland
¹⁰ Space Telescope Science Institute, 3700 San Martin Drive, Baltimore, MD 21218, USA
¹¹ Department of Astrophysical Sciences, Princeton University, Peyton Hall, Princeton, NJ 08544, USA
¹² Canada–France–Hawaii Telescope Corporation, 65-1238 Mamalahoa Hwy, Kamuela, HI 96743, USA
¹³ Department of Physics and Astronomy, The Johns Hopkins University Homewood Campus, Baltimore, MD 21218, USA
¹⁴ Institute für Theoretische Physik, Universität Zürich, Winterthurerstrasse 190, CH-8057 Zürich, Switzerland
¹⁵ Astronomy Department, University of Michigan, Ann Arbor, MI 48109, USA

APPENDIX A: PROPERTIES OF GALAXIES

Fig. A1 shows various physical properties of galaxies: V/σ , sSFR, $g-r$ colour and age as a function of the stellar mass at $z = 1.83$. There are correlations between the stellar kinematics V/σ and galaxy masses: more massive galaxies are pressure supported; their sSFR and mass: more massive galaxies have lower sSFR, i.e. are more passive; their colour and mass: more massive galaxies are redder; and their age and mass: more massive galaxies are older. Note the quite large scatter at all masses, that is more pronounced for lower mass objects, which can be explained by the fact that low-mass field galaxies in low-density environments evolve differently from low-mass satellites galaxies in high-density environments.

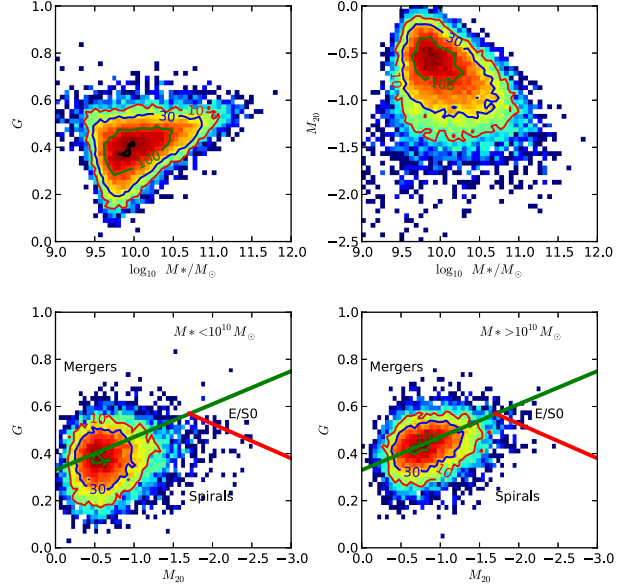


Figure A2. Bivariate distributions of stellar mass, Gini (G) and M_{20} morphological parameters for galaxies in the simulation at $z = 1.8$ in the rest-frame u filter. Lower panels show the Gini– M_{20} distributions for stellar mass selected samples. The zones for elliptical, spiral and merger galaxies are schematically drawn as tentative locations of local ellipticals, spirals and mergers at $z \simeq 2$. See the text for details.

Fig. A2 shows the relation between M_s and the morphology parameters Gini and M_{20} measured in the rest-frame u band. These morphological estimators allow in principle to separate spirals from spheroids, ellipticals, and merging galaxies. This has been done in the local universe (Lotz et al. 2004) and at higher redshift (Abraham et al. 2007; Lotz et al. 2008; Lee et al. 2013). The regions drawn in the figure are taken from Lotz et al. (2008). Their precise locations with respect to the distributions measured here should be taken with caution: extinction by dust is not taken into account, morphological k -corrections (although quite small) are not accounted for and the spatial resolution is not matched. Despite all these caveats which may explain the relatively small number of galaxies classified as ellipticals or spheroids from these diagrams, there seems to be, qualitatively, rather good agreement between the distributions measured in the deep surveys and in the simulation.

APPENDIX B: GRID-LOCKING

Fig. B1 displays a Mollweide projection of the orientations of *galaxy* spins along Cartesian axes, for a range of halo mass. Galaxies hosted by haloes lighter or heavier than $5 \times 10^{11} M_\odot$ are considered. While the spins of the less massive galaxies are clearly aligned with the grid, no obvious alignment is seen for the high-mass galaxies. Lighter galaxies are preferentially locked with the grid because they are composed of very few grid elements: the gaseous disc of a galaxy with $\sim 10^9 M_\odot$, embedded in a halo of mass $\sim 10^{11} M_\odot$, tends to be aligned with one of the Cartesian axes due to the anisotropic numerical errors. However, for

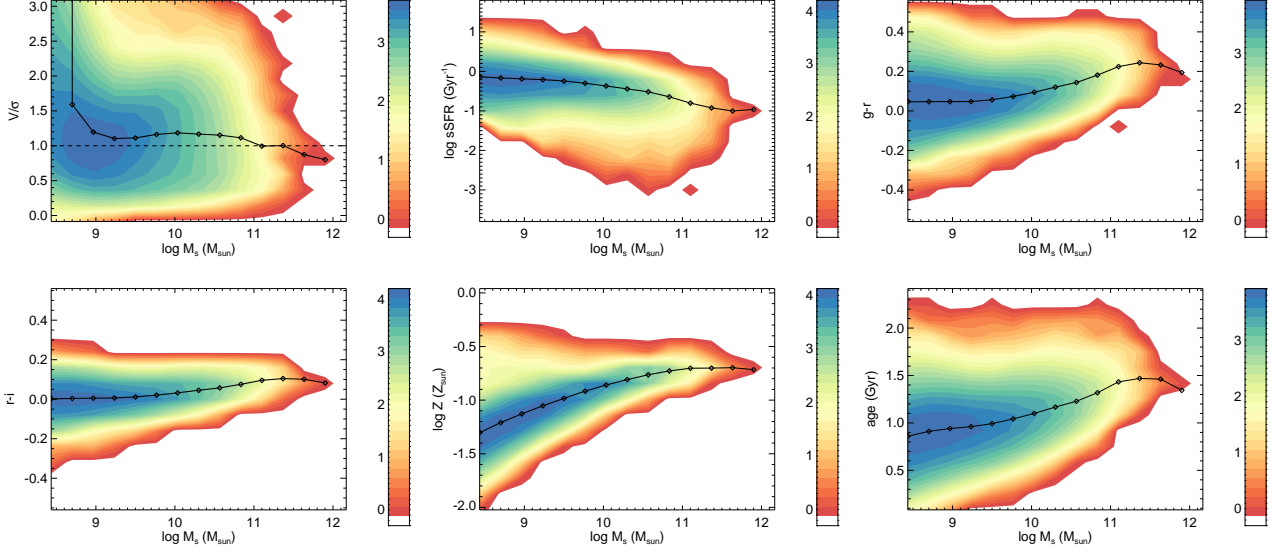


Figure A1. From top to bottom and left to right: Contours of the logarithmic number of galaxies for 2D projected kinematics of the stars V/σ , sSFR, $g-r$ colour, $r-i$ colour, metallicity Z and age as a function of the stellar mass of the galaxy at $z = 1.83$. The solid lines with diamonds correspond to the average values as a function of the stellar mass. The dashed line in the top-left panel corresponds to $V/\sigma = 1$.

more massive galaxies, the grid-locking is absent due to a larger number of resolution elements to describe those objects. This result is consistent with that of Hahn et al. (2010) and Danovich et al. (2012).

Fig. B2 shows the distribution of the axis of all the elements of the skeleton on the sphere. There is no preferential direction of alignment with respect to the box axes.

Low-mass galaxies (within halo of mass $< 5 \times 10^{11} M_\odot$) show some preferential alignment along the x -, y - and z -axis of the simulation box. In order to evaluate the effect of grid-locked galaxies on the galaxy-filament alignment signal, we have removed galaxies whose spin is comprised within less than 10° of any of the Cartesian planes of the box. Fig. B3 shows that the alignment signal without grid-locked galaxies is comparable to the case where all galaxies are accounted for. Low-mass galaxies have spin preferentially aligned with their filament, and massive galaxies have a spin perpendicular to the filament with a transition mass between $10^{10.25}$ and $10^{10.75} M_\odot$. This behaviour is expected as filaments do not suffer from grid-locking; the effect of grid-locking on low-mass galaxies brings some extra noise to the alignment measurement. Thus, the signal obtained for alignment of low-mass galaxies, while probably underestimated, is a robust trend. The same is true for high-mass galaxies that do not suffer from spurious grid-locking.

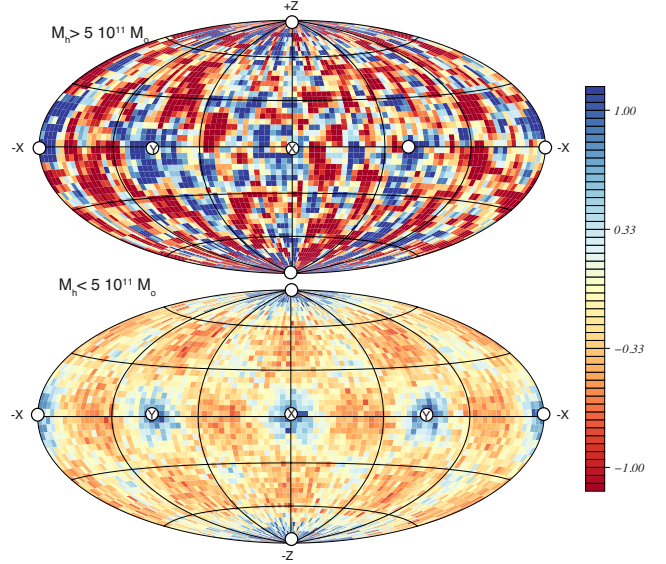


Figure B1. The effect of grid-locking at redshift $z = 1.3$ of the spin of galaxies for haloes more (top panel), respectively less (bottom panel) massive than $5 \times 10^{11} M_\odot$ respectively. The white discs represent the directions of the simulation box as labelled. The colour coding represents relative fluctuations around the mean. The smaller galaxies (bottom panel) show a clear sign of grid-locking, while the more massive sample (top panel) does not.

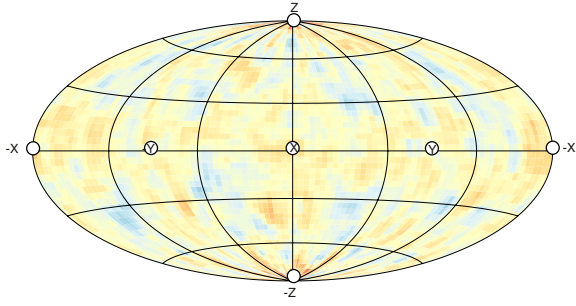


Figure B2. The effect of grid-locking of the skeleton segments at $z = 1.3$. The colour coding is the same as in Fig. B1. No preferred direction is shown for the skeleton.

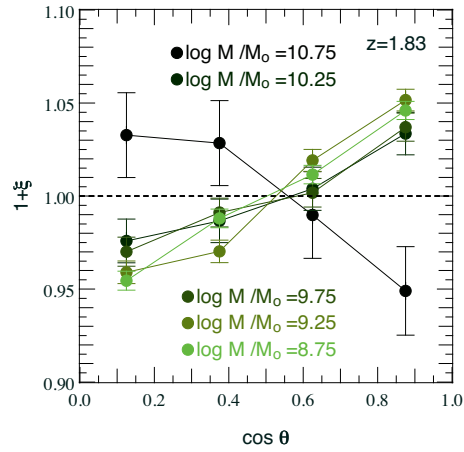


Figure B3. Excess probability ξ of the alignment between the spin of galaxies and their filament for galaxies with different stellar masses. Galaxies whose spin is contained within an angle smaller than 10 degrees from any cartesian planes of the box are not taken into account. Dashed line is the zero excess probability $\xi = 0$.